Geometric constraints on phase coexistence in vanadium dioxide single crystals

2017 Nanotechnology 28 085701

(http://iopscience.iop.org/0957-4484/28/8/085701)

IOP Publishing Nanotechnology
Nanotechnology 28 (2017) 085701 (9pp) doi:10.1088/1361-6528/aa5652

Geometric constraints on phase coexistence in vanadium dioxide single crystals

Christina McGahan[1], Sampath Gamage[2,3], Jiran Liang[1,4], Brendan Cross[2,3], Robert E Marvel[5,6], Richard F Haglund[1,5] and Yohannes Abate[2,3]

[1] Department of Physics and Astronomy, Vanderbilt University, Nashville, TN 37235-1807, United States
[2] Center for Nano-Optics (CeNO), Georgia State University, Atlanta, GA 30303, United States
[3] Department of Physics and Astronomy, Georgia State University, Atlanta, GA 30303, United States
[4] School of Electronics and Information Engineering, Tianjin University, Tianjin 300072, People's Republic of China
[5] Interdisciplinary Materials Science Program, Vanderbilt University, Nashville, TN 37235-1406, United States
[6] Currently at Thermo Fisher Scientific, Guilford, CT 06437, United States

E-mail: richard.haglund@vanderbilt.edu and yabate@gsu.edu

Received 12 October 2016, revised 12 December 2016
Accepted for publication 3 January 2017
Published 18 January 2017

Abstract

The appearance of stripe phases is a characteristic signature of strongly correlated quantum materials, and its origin in phase-changing materials has only recently been recognized as the result of the delicate balance between atomic and mesoscopic materials properties. A vanadium dioxide (VO_2) single crystal is one such strongly correlated material with stripe phases. Infrared nano-imaging on low-aspect-ratio, single-crystal VO_2 microbeams decorated with resonant plasmonic nanoantennas reveals a novel herringbone pattern of coexisting metallic and insulating domains intercepted and altered by ferroelastic domains, unlike previous reports on high-aspect-ratio VO_2 crystals where the coexisting metal/insulator domains appear as alternating stripe phases perpendicular to the growth axis. The metallic domains nucleate below the crystal surface and grow towards the surface with increasing temperature as suggested by the near-field plasmonic response of the gold nanorod antennas.

Keywords: vanadium dioxide, plasmonics, phase transition, stripe phases, ferroelastic domains

(Some figures may appear in colour only in the online journal)

1. Introduction

Ordered phase separation during an electronic or magnetic phase transition is a characteristic signature of strongly correlated materials, such as those that exhibit colossal magnetoresistance and high-temperature superconductivity [1–3]. Cuprates—for example, neodymium- and sodium-doped high-temperature superconductors—form alternating stripes and checkerboard patterns of coexisting phases [1, 2]. Stripes of metallic and insulating phases with long-range order form during the electronic phase transition in organic charge-transfer complexes with spatial periods in the single-micrometer regime [2, 4]. Vanadium dioxide (VO_2) is a canonical strongly correlated material, and an excellent candidate for studies of phase coexistence, as it is undergoes an insulator-to-metal (IMT) phase transition near room temperature accompanied by a first-order structural phase transition from monoclinic to rutile crystal structure, leading to large resistivity and permittivity changes [2]. The phase transition can be induced thermally [5, 6], by electric field [7, 8], or optically on ultrafast time scales [9, 10].

Single crystals of VO_2 do in fact exhibit coexisting, ordered metallic (M) and insulating (I) domains in thermal equilibrium that have been observed using scattering-scanning near-field optical microscopy (s-SNOM) [11, 12], pump-probe s-SNOM [13, 14], scanning near-field microwave microscopy [15, 16], and optical microscopy [15, 17]. Coexisting, ordered monoclinic (M1 and/or M2) or triclinic (T) and rutile (R) domains have been observed in thermal equilibrium via Raman spectroscopy [14, 16, 18, 19], with

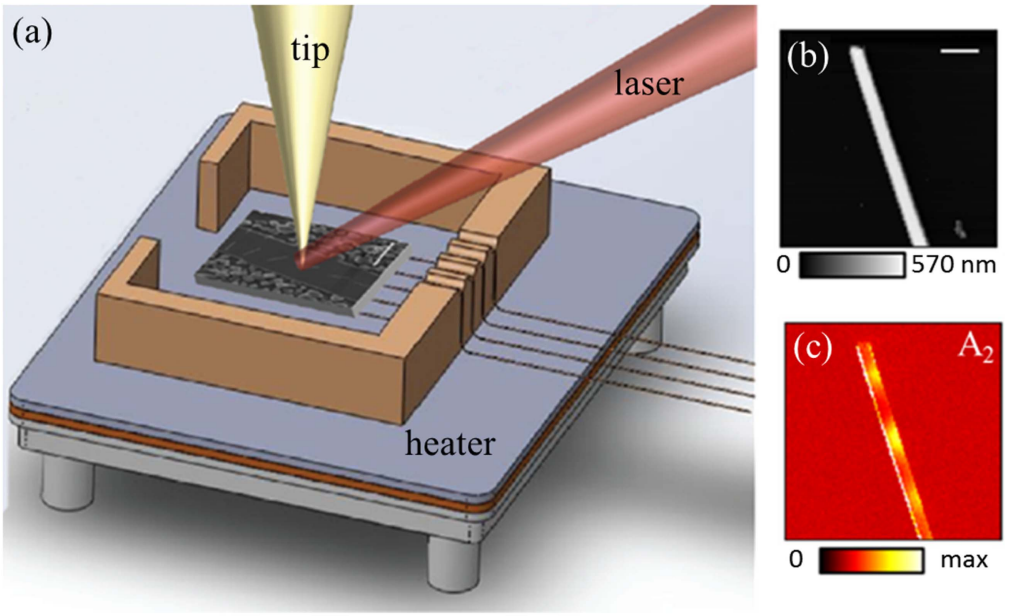

Figure 1. Schematic of the s-SNOM setup (a), topographic (b) and second harmonic near-field amplitude (c) images of a single crystal VO_2 nanobeam grown on sapphire substrate recorded at temperature 50 °C and laser wavelength, $\lambda = 10.7\ \mu$m. Scale bar at top of (b) represents 50 nm and applies to (b) and (c). Optical amplitude image of the strained beam displays the formation of coexisting metallic (bright) and insulating (dark) domains even below the critical temperature.

insulating VO_2 observed to have M1, M2 or T crystal structure and metallic VO_2 observed to have a rutile crystal structure. Rutile and M1 structural domains have been shown to correspond with the locations of coexisting M and I domains imaged with reflected white light, respectively [20]. Transient coexisting metallic and insulating domains have also been observed in nanobeams using optical pump-THz probe s-SNOM even below the fluence threshold required to initiate the completed phase transition [14]. Ordered phase coexistence of stripes perpendicular to the c_R axis or in a herringbone structure has also been observed in cracked epitaxial VO_2 films on TiO_2 which form ribbons [21–23] as well as single crystals both on their growth substrate [12, 15–17, 24, 25] and clamped on a different substrate [18] due to strain. However, with a single exception in the literature [25], these experiments have been carried out on micro- or nanobeams with high aspect ratios and until now, no one has looked in detail at the critical issue of stripe phases in geometries with low aspect ratios typical of bulk single crystals.

Here, we describe observations of the phase transition in VO_2 single crystals using s-SNOM and polarized far-field optical microscopy and probe for the first time an altered herringbone pattern of coexisting M and I domains. We compare the ordered phase coexistence of VO_2 in strained nanobeams and microbeams and see aspect-ratio-dependent patterns via s-SNOM. In the case of low-aspect-ratio microbeams, we find that deviations from the herringbone structure are due to ferroelastic domains [16]. Using polarized optical microscopy, we can image these ferroelastic domain walls with mechanisms of contrast described in [16, 19]. Combining s-SNOM and polarized optical microscopy, we show that a VO_2 single crystal responds to strain by (1) forming ferroelastic domains and (2) nucleating and growing M/I stripe phases. We propose that this herringbone pattern of M/I phase coexistence is related to the absence of an aspect-ratio-related geometric constraint [22, 25] and to substrate-induced strain that is relieved by the formation of ferroelastic domains [16]. In high-aspect-ratio nanobeams, we reproduce the well-known perpendicular stripe pattern [12].

These inhomogeneities are of interest because strongly correlated materials can be used for active plasmonics by capitalizing on the differing local dielectric functions associated with the phase transitions [26–28]. To probe the interaction between the coexisting domains and metal plasmons on the surface of a single crystal, we decorate the microbeam with resonant dipole nanoantennas. However, in contrast to previous studies on thin films where nanorods are in direct contact with the VO_2 [28], we observe no interaction between the plasmon and the metallic domains in the VO_2. This indicates that the *local* dielectric environment of the nanoantenna—the plasmon near field with a range of a few tens nanometers—is not modified by the metal and insulating domains which form during the IMT.

2. Materials and methods

We examined coexisting M and I phases in VO_2 single crystals during the thermally induced IMT using a commercial (neaspec.com) s-SNOM integrated with a laboratory-built heater (figure 1(a)). A platinum–iridium-coated atomic force microscope (AFM) tip, oscillating at a resonance frequency of 280 KHz, was illuminated by a focused CO_2 laser ($\lambda = 10.7\ \mu$m) at 45° with respect to the sample surface [29, 30]. The excitation laser was polarized perpendicular to the plane of incidence (s-polarized) and the scattered signal

was detected in the plane of incidence (p-polarized). The scattered signal from the tip-sample interface was demodulated at higher harmonics of the tip frequency to suppress background and detected via pseudoheterodyne interferometry. By raster scanning the sample surface, concurrent topographical (figure 1(b)) and near-field optical (figure 1(c)) images of VO_2 single crystals and Au nanoantennas were recorded as a function of temperature. Vanadium dioxide switches from I to M at an applied electric field of order $2–7 \times 10^7$ V m^{-1} [7, 31] and also when exposed to a picosecond pulse of alternating current terahertz electric field with a peak value of 1×10^8 V m^{-1} [8], both of which are initiated and driven by the Poole–Frenkel effect. These threshold values are orders of magnitude higher than the 6×10^5 V m^{-1} electric field of the CO_2 laser used to excite the plasmon.

The topographic image of a VO_2 nanobeam (figure 1(b)) shows a uniform crystal, free of defects and grain boundaries, indicating that the optical contrast in figure 1(c) is not due to the existence of multiple grains. The strong contrast in scattering amplitude in s-SNOM at 10.7 μm is due to local variations in the polarizability of the sample [28, 29] from differences between the optical constants of VO_2 in M and I regions. From ellipsometry, we measure $\varepsilon_1 = 2.4$ and $\varepsilon_2 = 2.9$ for I VO_2 and $\varepsilon_1 = -3.3$ and $\varepsilon_2 = 45$ for M VO_2. Based upon the VO_2 optical constants, the M regions are expected to have strong scattering amplitudes due to the large negative ε_1 and large positive ε_2, whereas I regions are expected to have weaker scattering amplitudes due to the moderate ε_1 and small ε_2 [32]. In this way, s-SNOM can image the phase coexistence in VO_2 using a CO_2 laser and M and I domains can be identified based upon their relative scattering amplitudes.

Figure 1(c) shows the s-SNOM amplitude image of a VO_2 nanobeam below the critical temperature for the IMT. Regions with strong scattering amplitudes are coded as bright (yellow) and correspond to scattering from metallic VO_2 domains, whereas regions with weak scattering amplitudes are assigned as dark (red) and correspond to insulating domains. Since s-SNOM images the local permittivity of the sample within the optical near-field of the tip at the excitation wavelength, the probe volume extends into the bulk of the crystal [29, 33–38] within the penetration depth of both insulating and metallic VO_2. Thus, at 10.7 μm, the s-SNOM is sensitive to the phases of VO_2 domains well below the surface of a single crystal.

We fabricated VO_2 single-crystal microbeams following the synthesis documented in [39] and [40]. The VO_2 crystals were grown on a silicon substrate covered with its native thermal oxide, typically 2 nm thick as measured by ellipsometry. The crystals were grown by physical vapor transport at 1.7 Torr and 825 °C in an argon gas environment for 1 h using vanadium pentoxide (V_2O_5) powder loaded upstream of a $10 \times 1 \times 1$ cm^3 crucible with substrates loaded between 5 and 7 cm downstream. Chromium alignment markers 200 μm apart were patterned photolithographically on the substrate after crystal growth, allowing specific crystals to be located by scanning electron microscopy (SEM) and s-SNOM. In preparation for electron beam lithography (EBL), PMMA 950 A4 was spun on the sample. The crystal chosen for this experiment has an aspect ratio of 5:1, which differs from that of the nanobeams examined in figures 1(b) and (c) and that of nanobeams with aspect ratios of order 20:1 examined in previous work with the exception of one previous study where a low-aspect-ratio crystal was imaged [25].

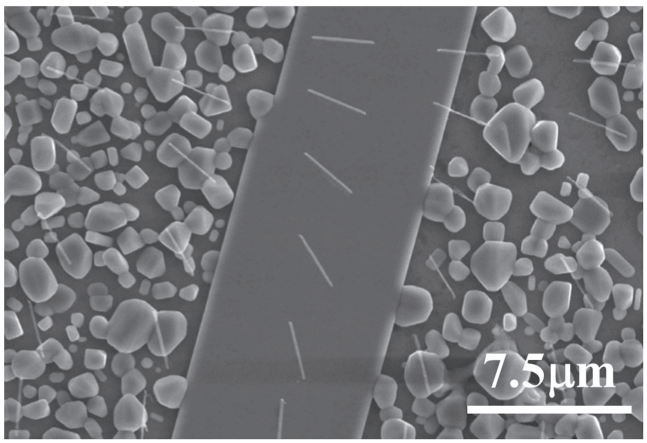

Figure 2. Scanning electron micrograph of VO_2 single-crystal microbeam grown on silicon substrate. Gold nanorods were fabricated on top of the single crystal via electron beam lithography.

Due to the strong contrast of the IMT in s-SNOM at mid infrared frequencies, the gold antennas (3.2 μm by 300 nm nominal dimensions) were designed to be resonant with 10.7 μm light and fabricated atop individual single crystals via EBL with a Raith eLINE system. After development of the photoresist by methyl isobutyl ketone:isopropyl alcohol, 50 nm of Au was deposited by thermal evaporation. The structures, shown in figure 2, resulted after liftoff in warm acetone on a stir plate. Identical Au rods were oriented on an individual single crystal at 18° angular increments over a 90° range of angles to permit in-plane polarization-dependent measurements, as the excitation laser in-plane polarization direction cannot be modified in this apparatus. Fabricating Au antennas resonant with the CO_2 laser also allowed for simultaneous imaging of the M/I phase coexistence and the Au plasmon resonance.

3. Results and discussion

We first investigated the insulating and metallic domains in narrow (~80 nm), high aspect ratio VO_2 single-crystal nanobeams (figure 3) grown by vapor phase transport [17, 24] on a sapphire substrate and observed the evolution of the coexisting phases in temperature. We verified the uniformity of the single crystals via topographic measurements (figure 3(a)). The nucleation of M phases during the IMT can begin at random locations on a single crystal, as in the onset of the IMT in polycrystalline thin films [32]. Due to the high-aspect-ratio and the crystallinity of nanobeams, strain at the crystal-substrate interface causes the domain structure to evolve by forming well-defined and periodic metallic rutile

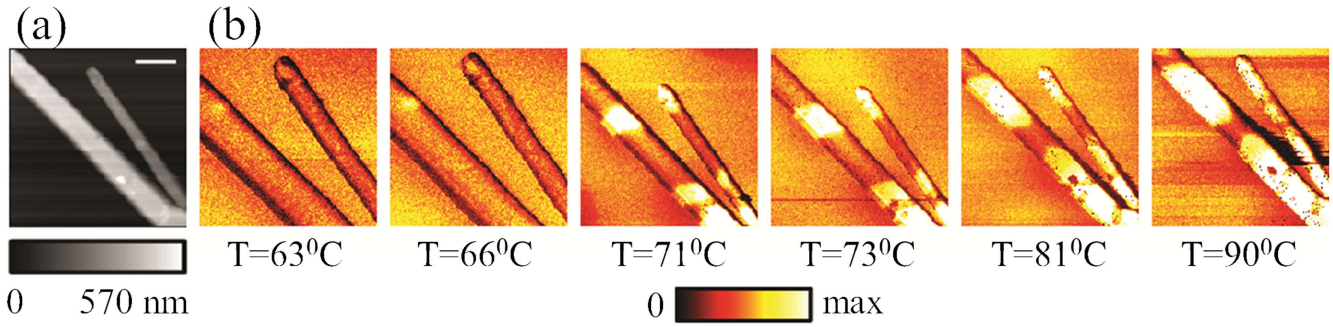

Figure 3. Topographic (a) and second harmonic near-field amplitude images (b) of single crystal VO_2 nanobeams with width less than 100 nm grown on sapphire substrate. Scale bars at top right of each panel represent 100 nm. The amplitude plots (b) show how the IMT evolves as a function of temperature, with insulating domains shown in orange (dark) and metallic domains shown in white (bright).

and insulating non-rutile domains perpendicular to the c_R (along the long dimension of the crystal) axis that span the width of the crystal [17]. At the onset of the IMT ($T_c \sim 63\,^{\circ}C$) in the nanobeams examined, bright metallic nanodomains form perpendicular to the c_R axis and grow in size as temperature increases, forming a periodic pattern of stripes evolving towards a dominating bright phase at high temperature ($T \sim 90\,^{\circ}C$, figure 3(b)). The ordered coexistence of M and I domains is ideal for determining the effect of the nanorod plasmon on the IMT; however, it is not feasible to fabricate 3.2 μm long Au nanorods resonant at the excitation laser wavelength on these nanobeams due to their narrow width.

To explore interactions of the Au nanoantennas with single crystal VO_2, we grew a VO_2 microbeam (estimated thickness 250–500 nm from tilted SEM) on Si that was wide enough (lateral dimension 8.5 μm) to allow for fabrication of 3.2 μm long dipole antennas resonant with the excitation laser. Figure 4 displays topographical (figure 4(a)), near-field amplitude (figure 4(b)), and polarized optical microscopy (figure 4(c)) images of Au antennas on this microbeam. The smooth topography in figure 4(a) indicates a uniform single crystal. As with nanobeams, stripes are seen in the amplitude image (figure 4(b)), indicating the formation of coexisting M and I domains in this microbeam. The gradations in brightness of the M stripes indicate variation in the M domain scattering signal which we suggest are caused by different M domains being buried at a variety of depths beneath I domains at crystal surface. This suggests that in figure 4(b), the rightmost metallic domain is farther from the crystal surface and buried deeper in an I domain than the bottom portion of the leftmost metallic domain because the bottom region of the leftmost domain exhibits more scattering than the rightmost metallic domain. The s-SNOM technique, however, is unsuitable for quantitatively probing the depths of buried domains as the scattering signal is generated from a nanoscale light source whose interaction with the phase change material within the source near field extends to depth which is difficult to predict and will change as the M domains grow.

In the low-aspect-ratio microbeam, metallic rutile and insulating non-rutile domains primarily form a herringbone pattern oriented at $50 \pm 5^{\circ}$ with respect to the c_R axis (marked in figure 4(a)). Mirror symmetry occurs in M1 VO_2 because both directions are energetically equivalent and correspond to the energy-equivalent orientations of the monoclinic c-axis (described in [22, 23] and observed in a VO_2 crystal in [25]). This ties the atomic scale response of VO_2 to mesoscale properties. We posit that the low aspect ratio of the microbeam is responsible for the observation of the herringbone pattern here and in [25] as opposed to the domain pattern of stripes perpendicular to the c_R axis observed in high-aspect-ratio nanobeams [12, 15–17, 24]. However, in the microbeam some M domain walls are oriented at $50 \pm 5^{\circ}$ with respect to the c_R axis in one region but bend to become perpendicular to the c_R axis, in a deviation from a pure herringbone pattern.

The deviations from the herringbone pattern are correlated with the positions of ferroelastic domains. Ferroelastic domains were first observed in VO_2 at room temperature using polarized far-field optical microscopy and scanning microwave microscopy to examine nanoplatelets comparable in width to the microbeam studied here [15, 16]. Ferroelastic domains were further examined at room temperature on single crystals with M1, M2, and T crystal structures, and confirmed by Raman spectroscopy [19]. These ferroelastic domains form in reaction to stress in the monoclinic phase of VO_2. In M1 VO_2, as the temperature is increased, the ferroelastic domains switch between energy-equivalent orientations of the same monoclinic crystal structure. The large-scale ferroelastic domain patterns that form in M1 VO_2 are related to the crystal width and the strength of the interaction between the crystal and the substrate [16]. The ferroelastic domains in M1 VO_2 and M/I stripe phases couple due to their mutual interaction with strain; walls between parallel-plane ferroelastic domains in M1 VO_2 oriented perpendicular to the c_R axis serve as nucleation sites for metallic rutile domains of VO_2 [16] which do not conform to the herringbone pattern of M/I phase coexistence.

Polarized optical microscopy of the VO_2 microbeam decorated with Au nanorods in figure 4(c) shows the positions of ferroelastic domains and nanoantennas on the crystal probed with s-SNOM in figures 4(a) and (b). The Au nanoantennas can be seen in figure 4(c) as narrow bright areas at locations corresponding to the bright regions in figure 4(a). The ferroelastic domains are manifest as bright rectangular regions and a dark background. As the ferroelastic domains

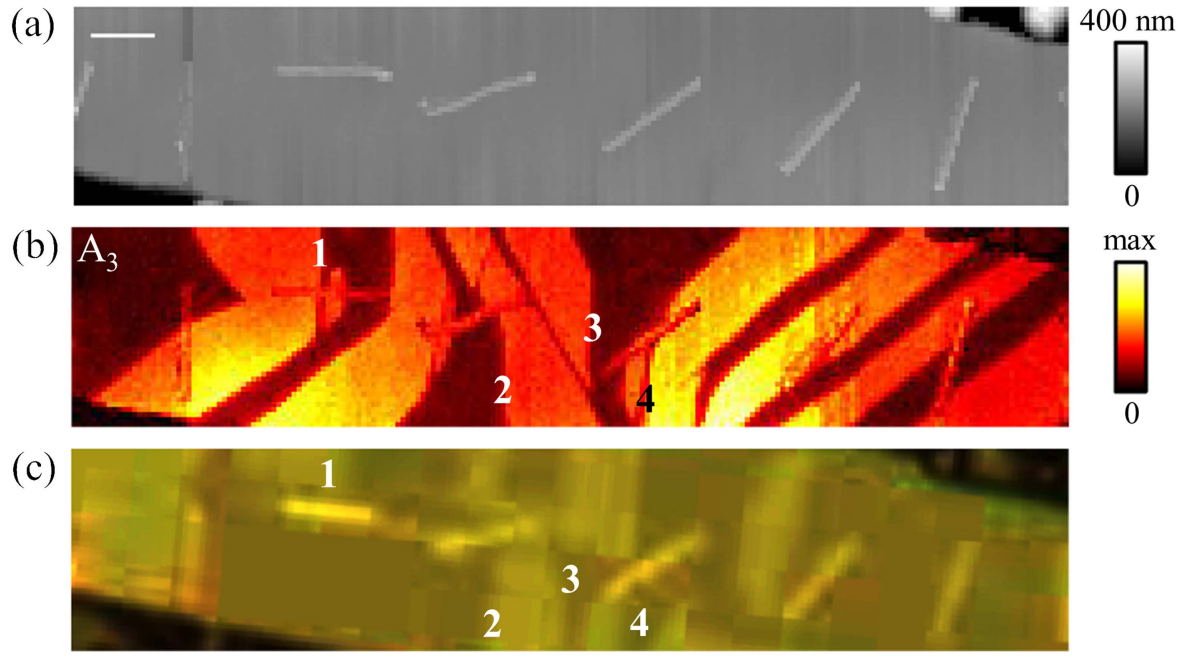

Figure 4. S-SNOM topography (a), second-harmonic near-field amplitude imaged at $T \sim 73$ °C and recorded at laser wavelength $\lambda = 10.7$ μm (b), and optical microscope (c) images of Au rods fabricated on a VO_2 microbeam grown on silicon. Scale bar at top right of (a) represents 1.5 μm. Arrow in (a) indicates the direction of the c_R axis in all three figures. Regions in (b) where the metallic domain walls deviate from the herringbone structure are labeled 1, 2, 3 and 4. Large alternating regions of bright and dark rectangles in (c) are ferroelastic domains. Ferroelastic domain walls corresponding to interruptions in the herringbone structure are labeled 1, 2, 3 and 4 to match the labels in (b).

are oriented perpendicular to the c_R axis of the microbeam, they are of the parallel-plane type and can serve as nucleation sites for metallic rutile domains [16]. The ferroelastic domain boundaries that nucleate metallic domains are marked in figure 4(c). These labels correspond to numerical labels in figure 4(b) which indicate locations where the herringbone structure is interrupted by metallic domains perpendicular to the c_R axis.

For example, consider the region marked '2' in figures 4(b) and (c). In figure 4(b), a domain wall located at '2' is oriented perpendicular to the c_R axis in the bottom half of the figure and oriented at $50 \pm 5°$ with respect to the c_R axis in the top half of the figure. The part of the domain wall oriented at $50 \pm 5°$ with respect to the c_R axis follows the herringbone pattern, but the domain wall labeled as '2' deviates from this pattern in the bottom part of the figure. In figure 4(c), there is a boundary between a bright and a dark ferroelastic domain at the location marked '2' running perpendicular to the c_R axis in the bottom half of the figure. This is evidence that the ferroelastic domain wall has nucleated the M/I domain wall labeled as '2'. By comparing numbered regions in figures 4(b) and (c), we see that the numbered ferroelastic domain walls line up with those M-I boundaries that differ from the herringbone structure. This indicates that the ferroelastic domains influence the formation of metallic rutile domains and thus cause deviation from the herringbone structure, as the metallic domain walls nucleated at each of the four numerically labeled positions would not have occurred if not for the ferroelastic domain wall at each labeled position.

Microbeams of VO_2 exhibit ordered, coexisting M and I phases that should in principle interact with plasmonic Au nanorods by altering the plasmon resonance frequency and thus the amplitude contrast observed via s-SNOM. Nevertheless, in figure 4(b), we do not observe detectable modification of the nanorod plasmon resonance. This indicates that Au nanorod antennas are not influenced by the phase coexistence, though the Au nanorods were simulated to be resonant with the exciting laser. This is unexpected given the quenching of the Au nanoantenna plasmon resonance seen in Au nanorod plasmons in direct contact with M domains of thin films [28]. We next explore the reasons for the lack of a plasmonic interaction using both experiments and simulations.

That the Au antennas are resonant with 10.7 μm light can be verified by examining their amplitude and phase response at room temperature using s-SNOM. When a nanorod antenna is oriented parallel to the laser polarization and resonant with the laser wavelength, the laser excites the plasmonic dipole mode of the rod, giving rise to a well-known amplitude and phase contrast at the rod ends [41]. Figure 5 shows experimental topographic (b), 2nd harmonic near-field optical amplitude (c), and phase (e) images of Au nanorods on a VO_2 microbeam taken at $\lambda = 10.7$ μm and at room temperature. The direction of the c_R axis is indicated in the SEM in figure 5(a). We observed the characteristic amplitude and phase contrast when the nanorod antenna and laser field are parallel, and at other rod orientations the dipolar signature is weak. This is expected due to the contribution from the metallized AFM tip used to image the IMT simultaneously

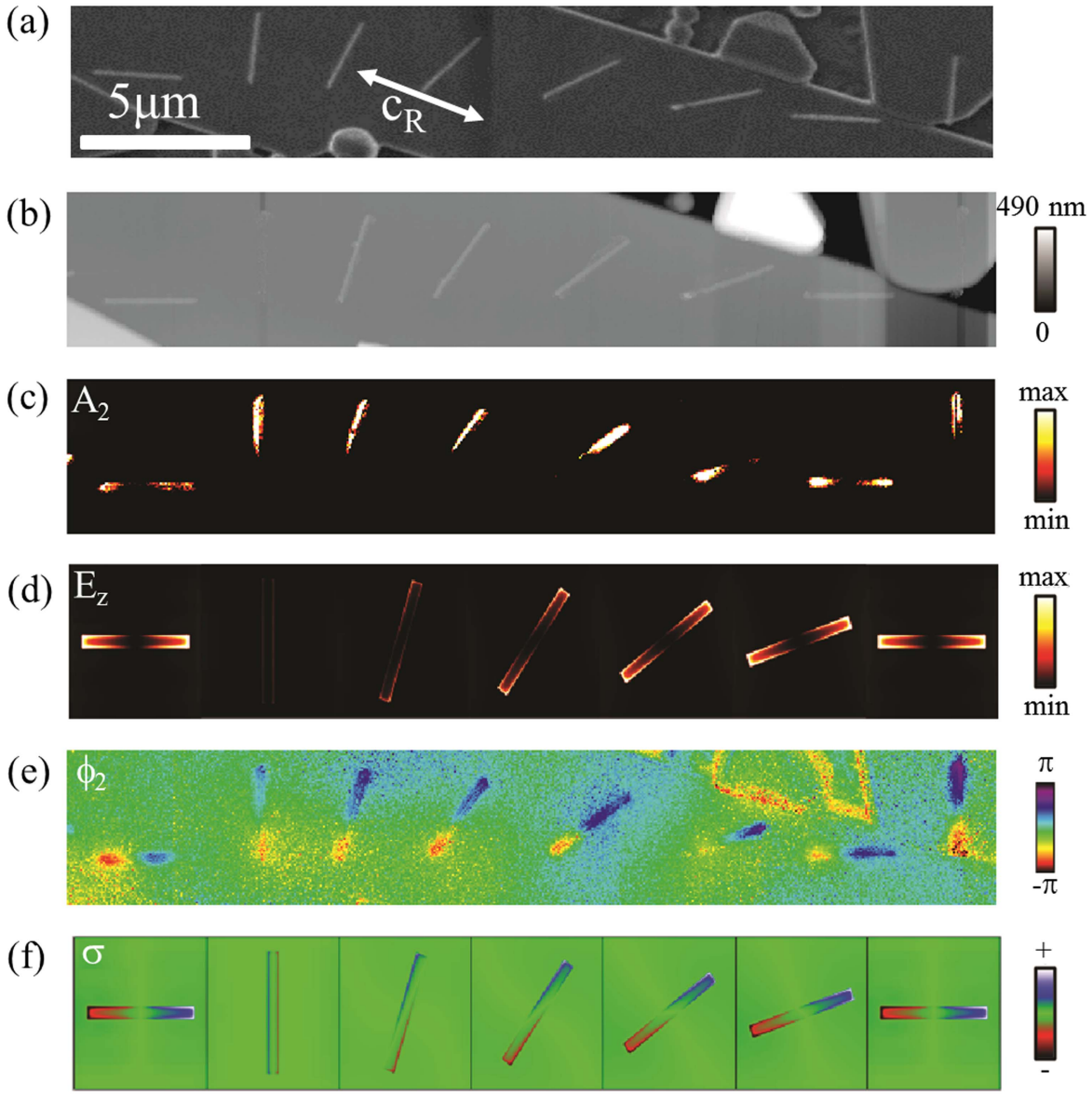

Figure 5. Images of the Au nanorod array: (a) SEM, (b) topographic, (c) experimental second harmonic near-field amplitude, (d) FDTD simulation of electric field amplitude, (e) experimental second harmonic phase, (f) and FDTD simulated phase images of Au antennas fabricated on a VO_2 single-crystal microbeam and recorded at room temperature. (c) and (e) were recorded while the microbeam was excited by a laser with $\lambda = 10.7$ μm. Arrow in (a) indicates the direction of the c_R axis in all six figures.

with the Au plasmons. As a result of strong local antenna-field distortions caused by the metallic AFM tip, even Au rods oriented perpendicular to the laser polarization showed bright optical amplitude and phase contrast. The orientation-dependent excitations were simulated using finite-difference, time-domain computations shown in figures 5(d) and (f), which exhibit decreased field intensity and reduced phase contrast at the nanorod ends, as the angle between the nanorod long axis and polarization of the laser is rotated from 0° to 90°. Taken together, these images indicate clearly that the antennas have resonant excitation wavelengths close to the incident 10.7 μm laser light.

Results from s-SNOM imply that the metallic rutile stripes in the microbeam form at the crystal-substrate interface and are not within the plasmon interaction range of the Au nanorods on the surface of the VO_2 as soon as the M domains nucleate. Though metallic domains more than several nanometers below the surface of the single-crystal microbeam can be probed using s-SNOM [29, 33–37], the metallic domains are too far beneath the crystal surface to interact with the Au nanorods due to the rapid decay of the out-of-plane plasmon field. Thus, the Au nanoantennas do not show the measurable quenching seen in previous thin film studies [28].

Figure 6 demonstrates this principle, showing the growth of M domains toward the top surface of the crystal as the temperature varies, how the difference between the s-SNOM probing depth and the maximum plasmon interaction depth alters the s-SNOM image formation, and how the dipole plasmon is altered by the IMT. Figure 6(a) represents a plasmon dipolar mode on top of the insulating phase of VO_2

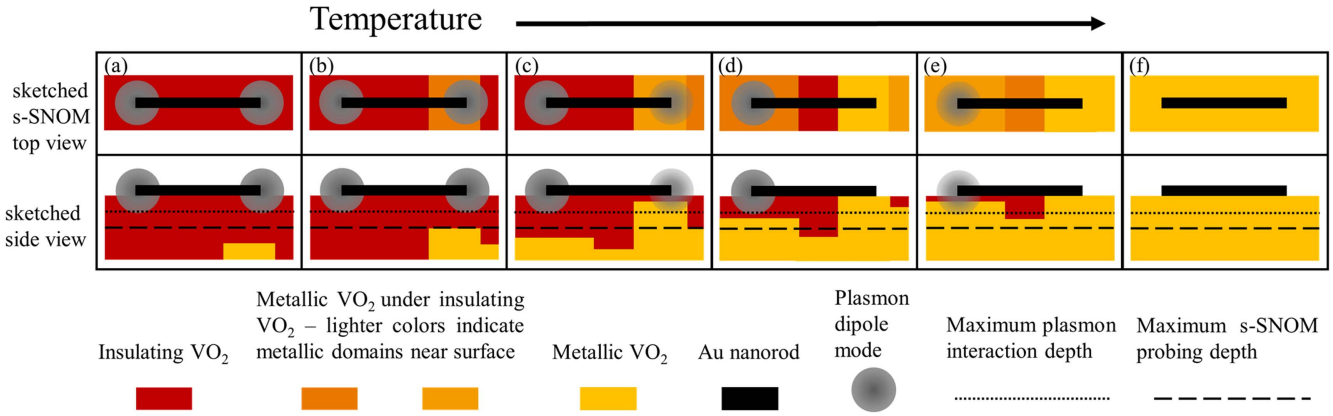

Figure 6. Schematic of Au nanorod on VO_2 crystal showing (top) the sketched s-SNOM image corresponding to (bottom) a given pattern of coexisting VO_2 phases in depth as a function of increasing temperature. The plasmon dipole mode, maximum plasmon interaction depth, and s-SNOM probing depth are superimposed on the depth-dependent diagrams. Electric field is parallel to the long axis of the nanorod shown in the s-SNOM top view. One metallic domain (a) out of range of s-SNOM and plasmon field, (b) in range of s-SNOM but not plasmon field, (c) in range of both s-SNOM and plasmon field. (d)–(f) Trend toward purely metallic VO_2 progresses.

with a M domain located far from the crystal surface and s-SNOM probe range. Increasing temperature (figure 6(b)) causes the metallic domain to grow nearer to the crystal surface and within the probing depth of s-SNOM but not within the metal nanorod plasmon interaction range, leaving the plasmon resonance unaltered from figure 6(a). The M domains imaged in figure 4(b) can be seen in this stage of growth, in range of the s-SNOM but not of the plasmons and thus the M domains do not alter the plasmon resonance. Further heating (figure 6(c)) brings a metallic domain into the plasmon interaction region, altering the plasmon resonance from that seen in figure 6(a), represented here as a decrease in the strength of the electric near field on the right side of the nanorod and a possible shifting of the plasmon resonance. This was observed for plasmonically resonant nanorods on VO_2 thin films [28]. The process continues in figure 6(d) with the electric near field on the right side of the nanorod being completely quenched and in figure 6(e) where the near field on the right is completely quenched and the near field on the left is weakened. In figure 6(f) the entire VO_2 crystal is metallic and the plasmon resonance corresponds to that which would be seen for the Au antenna on metallic VO_2, completing the process. Our observation that metallic domains nucleate beneath the crystal surface is further supported by three-dimensional s-SNOM imaging of VO_2 polycrystalline ribbons thinner than our 250–500 nm microbeams, being only 30–300 nm thick [22]. Metallic rutile domains were shown to preferentially nucleate at the VO_2-substrate interface to reduce the strain, which is the highest at the interface. The metallic domains were observed to grow towards the surface of the VO_2 and only occasionally appeared as stripes on the polycrystalline ribbon surface [22].

A logical future step would be to investigate the interaction of plasmons with few nanometer thick VO_2 single crystals such that Au nanoparticle plasmons would be sensitive to M domains even at the crystal-substrate interface and act as local probes. Etching methods, as recently described in [42], have been used to reduce the thickness of VO_2 thin films. These methods or any others have not been tested to thin VO_2 single crystals where undesirable etching of the sides of single crystals must be considered in addition to the desirable etching of the top of the crystal so to thin the crystal while preserving the footprint of the crystal. Significant process development would be needed to adapt these etching methods for the purpose of thinning but not shrinking VO_2 single crystals while maintaining crystals free of grain boundaries and switching VO_2. The M domains in thinner crystals than considered in the current work could also be detected by s-SNOM as soon as the domains nucleate and modify the gold plasmons on the surface of the crystal.

4. Conclusions

For the first time, we have studied the thermally induced IMT and the structure of the phase coexistence in a low-aspect-ratio VO_2 single-crystal microbeam decorated with plasmonic Au nanorod antennas to examine the inhomogeneous response of the crystal to the insulator-to-metal transition. We observe a herringbone-like M/I phase coexistence pattern with deviations due to ferroelastic domains, confirming that a phase coexistence pattern other than the commonly observed stripe pattern perpendicular to the c_R axis is possible in VO_2 single crystals and that the pattern observed may be determined by the crystal aspect ratio. These experimental measurements also suggest a connection between the M/I phase coexistence seen in strained epitaxial thin film ribbons and single crystals of VO_2. We observe that the herringbone structure is modified by the presence of ferroelastic domain walls that serve as nucleation sites for those M phase regions that deviate clearly from the herringbone pattern. This interaction cannot be seen in the polycrystalline VO_2 ribbons.

Decoration of single crystals with resonant Au plasmonic nanostructures establishes the possibility of using nanostructures as non-destructive plasmon probes of the VO_2 phase coexistence in the bulk of the crystal to compliment s-SNOM measurements. Using the Au nanorod plasmon resonance, we demonstrate depth-dependent inhomogeneity in VO_2 single

crystals because M domains nucleate beneath the VO_2 crystal surface and do not immediately extend throughout the entire depth of the crystal. With sufficiently thin single crystals, the M domains would be within the range of the plasmon field as they nucleate. Thus, the plasmon could serve as a non-invasive probe of the growth of M domains with temperature due to the temperature-dependent growth of M domains modifying the local dielectric environment of the plasmon in a manner detectable via s-SNOM.

Acknowledgments

CM was supported by the Office of Science, Department of Energy (DE-FG02-01ER454916) for the nanofabrication and computer simulations. REM developed the growth protocol for the larger single crystals, supported by the National Science Foundation (DMR-120507). JL was supported for experimental studies of VO_2 nanostructures at Vanderbilt by the State Scholarship Fund of China Scholarship Council (Grant No. 201406255081) and grew the larger crystals used in this study. YA acknowledges support from Research Corporation for Science Advancement, Scialog: Collaborative Innovation Award (ID# 23464). SG acknowledges support by the National Science Foundation under grant no. 1553251. BC acknowledge support of a grant from the Air Force Office of Scientific Research (FA9559-16-1-0172). The samples were fabricated and characterized in facilities funded by the National Science Foundation under the American Recovery and Reinvestment Act (NSF ARI-R2 DMR-0963361). We thank Claire Marvinney for helpful discussions about ferroelastic domain walls. We thank Kent Hallman for tilted SEM images of single crystals.

References

[1] Dagotto E 2005 Complexity in strongly correlated electronic systems *Science* **309** 257–62
[2] Basov D N, Averitt R D, van der Marel D, Dressel M and Haule K 2011 Electrodynamics of correlated electron materials *Rev. Mod. Phys.* **83** 471–541
[3] Imada M, Fujimori A and Tokura Y 1998 Metal-insulator transitions *Rev. Mod. Phys.* **70** 1039–263
[4] Okimoto Y, Kumai R, Saitoh E, Izumi M, Horiuchi S and Tokura Y 2004 Spectroscopic study of stripe pattern formation induced by current injection in a charge-transfer complex *Phys. Rev.* B **70** 115104
[5] Suh J Y, Lopez R, Feldman L C and Haglund R F 2004 Semiconductor to metal phase transition in the nucleation and growth of VO_2 nanoparticles and thin films *J. Appl. Phys.* **96** 1209–13
[6] Dicken M J, Aydin K, Pryce I M, Sweatlock L A, Boyd E M, Walavalkar S, Ma J and Atwater H A 2009 Frequency tunable near-infrared metamaterials based on VO_2 phase transition *Opt. Express* **17** 18330–9
[7] Markov P, Marvel R E, Conley H J, Miller K J, Haglund R F and Weiss S M 2015 Optically monitored electrical switching in VO_2 *ACS Photonics* **2** 1175–82
[8] Liu M *et al* 2012 Terahertz-field-induced insulator-to-metal transition in vanadium dioxide metamaterial *Nature* **487** 345–8
[9] Wegkamp D and Stähler J 2015 Ultrafast dynamics during the photoinduced phase transition in VO_2 *Prog. Surf. Sci.* **90** 464–502
[10] Cavalleri A, Dekorsy T, Chong H H W, Kieffer J C and Schoenlein R W 2004 Evidence for a structurally-driven insulator-to-metal transition in VO_2: a view from the ultrafast timescale *Phys. Rev.* B **70** 161102
[11] O'Callahan B T, Jones A C, Hyung Park J, Cobden D H, Atkin J M and Raschke M B 2015 Inhomogeneity of the ultrafast insulator-to-metal transition dynamics of VO_2 *Nat. Commun.* **6** 6849
[12] Jones A C, Berweger S, Wei J, Cobden D and Raschke M B 2010 Nano-optical investigations of the metal−insulator phase behavior of individual VO_2 microcrystals *Nano Lett.* **10** 1574–81
[13] Dönges S A, Khatib O, O'Callahan B T, Atkin J M, Park J H, Cobden D and Raschke M B 2016 Ultrafast nanoimaging of the photoinduced phase transition dynamics in VO_2 *Nano Lett.* **16** 3029–35
[14] Huber M A, Plankl M, Eisele M, Marvel R E, Sandner F, Korn T, Schüller C, Haglund R F, Huber R and Cocker T L 2016 Ultrafast mid-infrared nanoscopy of strained vanadium dioxide nanobeams *Nano Lett.* **16** 1421–7
[15] Tselev A, Strelcov E, Luk'yanchuk I A, Budai J D, Tischler J Z, Ivanov I N, Jones K, Proksch R, Kalinin S V and Kolmakov A 2010 Interplay between ferroelastic and metal−insulator phase transitions in strained quasi-two-dimensional VO_2 nanoplatelets *Nano Lett.* **10** 2003–11
[16] Tselev A, Meunier V, Strelcov E, Shelton W A, Luk'yanchuk I A, Jones K, Proksch R, Kolmakov A and Kalinin S V 2010 Mesoscopic metal−insulator transition at ferroelastic domain walls in VO_2 *ACS Nano* **4** 4412–9
[17] Cao J *et al* 2009 Strain engineering and one-dimensional organization of metal-insulator domains in single-crystal vanadium dioxide beams *Nat. Nanotechnol.* **4** 732–7
[18] Zhang S, Chou J Y and Lauhon L J 2009 Direct correlation of structural domain formation with the metal insulator transition in a VO_2 nanobeam *Nano Lett.* **9** 4527–32
[19] Strelcov E, Tselev A, Ivanov I, Budai J D, Zhang J, Tischler J Z, Kravchenko I, Kalinin S V and Kolmakov A 2012 Doping-based stabilization of the M2 Phase in free-standing VO_2 nanostructures at room temperature *Nano Lett.* **12** 6198–205
[20] Zhang S, Kim I S and Lauhon L J 2011 Stoichiometry engineering of monoclinic to rutile phase transition in suspended single crystalline vanadium dioxide nanobeams *Nano Lett.* **11** 1443–7
[21] Liu M K *et al* 2013 Anisotropic electronic state via spontaneous phase separation in strained vanadium dioxide films *Phys. Rev. Lett.* **111** 096602
[22] Liu M *et al* 2014 Symmetry breaking and geometric confinement in VO_2: results from a three-dimensional infrared nano-imaging *Appl. Phys. Lett.* **104** 121905
[23] Liu M *et al* 2015 Phase transition in bulk single crystals and thin films of VO_2 by nanoscale infrared spectroscopy and imaging *Phys. Rev.* B **91** 245155
[24] Atkin J M, Berweger S, Chavez E K, Raschke M B, Cao J, Fan W and Wu J 2012 Strain and temperature dependence of the insulating phases of VO_2 near the metal-insulator transition *Phys. Rev.* B **85** 020101
[25] Strelcov E, Lilach Y and Kolmakov A 2009 Gas sensor based on metal−insulator transition in VO_2 nanowire thermistor *Nano Lett.* **9** 2322–6

[26] Zheludev N I and Kivshar Y S 2012 From metamaterials to metadevices *Nat. Mater.* **11** 917–24
[27] Michel A K U, Chigrin D N, Mass T W W, Schonauer K, Salinga M, Wuttig M and Taubner T 2013 Using low-loss phase-change materials for mid-infrared antenna resonance tuning *Nano Lett.* **13** 3470–5
[28] Abate Y, Marvel R E, Ziegler J I, Gamage S, Javani M H, Stockman M I and Haglund R F 2015 Control of plasmonic nanoantennas by reversible metal-insulator transition *Sci. Rep.* **5** 13997
[29] Nuño Z, Hessler B, Ochoa J, Shon Y-S, Bonney C and Abate Y 2011 Nanoscale subsurface-and material-specific identification of single nanoparticles *Opt. Express* **19** 20865–75
[30] Keilmann F and Hillenbrand R 2004 Near-field microscopy by elastic light scattering from a tip *Phil. Trans. R. Soc.* A **362** 787–805
[31] Wu B, Zimmers A, Aubin H, Ghosh R, Liu Y and Lopez R 2011 Electric-field-driven phase transition in vanadium dioxide *Phys. Rev.* B **84** 241410
[32] Qazilbash M M *et al* 2007 Mott transition in VO_2 revealed by infrared spectroscopy and nano-imaging *Science* **318** 1750–3
[33] Engelhardt A P, Hauer B and Taubner T 2013 Visibility of weak contrasts in subsurface scattering near-field microscopy *Ultramicroscopy* **126** 40–3
[34] Krutokhvostov R, Govyadinov A A, Stiegler J M, Huth F, Chuvilin A, Carney P S and Hillenbrand R 2012 Enhanced resolution in subsurface near-field optical microscopy *Opt. Express* **20** 593–600
[35] Hauer B, Engelhardt A P and Taubner T 2012 Quasi-analytical model for scattering infrared near-field microscopy on layered systems *Opt. Express* **20** 13173–88
[36] Taubner T, Keilmann F and Hillenbrand R 2005 Nanoscale-resolved subsurface imaging by scattering-type near-field optical microscopy *Opt. Express* **13** 8893–9
[37] Govyadinov A A, Mastel S, Golmar F, Chuvilin A, Carney P S and Hillenbrand R 2014 Recovery of permittivity and depth from near-field data as a step toward infrared nanotomography *ACS Nano* **8** 6911–21
[38] Zhu J, Hippalgaonkar K, Shen S, Wang K, Abate Y, Lee S, Wu J, Yin X, Majumdar A and Zhang X 2014 Temperature-gated thermal rectifier for active heat flow control *Nano Lett.* **14** 4867–72
[39] Guiton B S, Gu Q, Prieto A L, Gudiksen M S and Park H 2005 Single-crystalline vanadium dioxide nanowires with rectangular cross sections *J. Am. Chem. Soc.* **127** 498–9
[40] Cheng C, Liu K, Xiang B, Suh J and Wu J 2012 Ultra-long, free-standing, single-crystalline vanadium dioxide micro/nanowires grown by simple thermal evaporation *Appl. Phys. Lett.* **100** 103111
[41] Mastel S, Grefe S E, Cross G B, Taber A, Dhuey S, Cabrini S, Schuck P J and Abate Y 2012 Real-space mapping of nanoplasmonic hotspots via optical antenna-gap loading *Appl. Phys. Lett.* **101** 131102
[42] Yamin T, Wissberg S, Cohen H, Cohen-Taguri G and Sharoni A 2016 Ultrathin films of VO_2 on r-cut sapphire achieved by postdeposition etching *ACS Appl. Mater. Interfaces* **8** 14863–70